JACS
JOURNAL OF THE AMERICAN CHEMICAL SOCIETY
pubs.acs.org/JACS
Article

Quasi-One-Dimensional Metallicity in Compressed $CsSnI_3$

Feng Ke, Jiejuan Yan, Roc Matheu, Shanyuan Niu, Nathan R. Wolf, Hong Yang, Ketao Yin,* Jiajia Wen, Young S. Lee, Hemamala I. Karunadasa, Wendy L. Mao, and Yu Lin*

Cite This: J. Am. Chem. Soc. 2022, 144, 23595−23602
Read Online
ACCESS | Metrics & More | Article Recommendations | Supporting Information

ABSTRACT: Low-dimensional metal halides exhibit strong structural and electronic anisotropies, making them candidates for accessing unusual electronic properties. Here, we demonstrate pressure-induced quasi-one-dimensional (quasi-1D) metallicity in δ-$CsSnI_3$. With the application of pressure up to 40 GPa, the initially insulating δ-$CsSnI_3$ transforms to a metallic state. Synchrotron X-ray diffraction and Raman spectroscopy indicate that the starting 1D chain structure of edge-sharing Sn−I octahedra in δ-$CsSnI_3$ is maintained in the high-pressure metallic phase while the SnI_6 octahedral chains are distorted. Our experiments combined with first-principles density functional theory calculations reveal that pressure induces Sn−Sn hybridization and enhances Sn−I coupling within the chain, leading to band gap closure and formation of conductive SnI_6 distorted octahedral chains. In contrast, the interchain I...I interactions remain minimal, resulting in a highly anisotropic electronic structure and quasi-1D metallicity. Our study offers a high-pressure approach for achieving diverse electronic platforms in the broad family of low-dimensional metal halides.

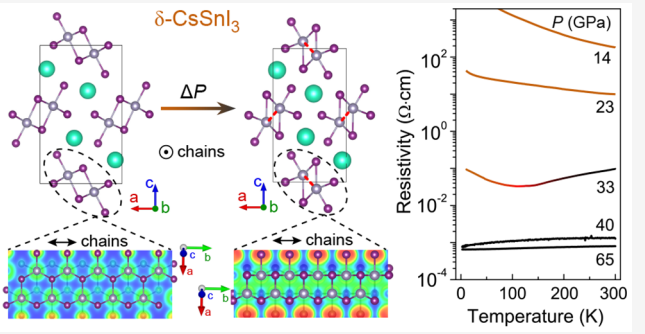

1. INTRODUCTION

Halide perovskites that have a chemical formula of ABX_3 represent an extensive family of materials with chemical and structural versatility. In these materials, the metal cation in the B site is coordinated by six halide anions to form a BX_6 octahedron with the A-site cation residing in the cavities defined by the corner-sharing BX_6 octahedra. The structural tunability of halide perovskites is also reflected in the ability to derive a wide variety of related, low-dimensional halide perovskites and analogous systems. For example, many 2D halide perovskites can be formed by inserting larger organic cations into the 3D perovskite structure along certain crystallographic directions.[1] Changing the metal-halide connectivity to face- or edge-sharing can also produce low-dimensional structures, such as those found in 1D δ-$(FA)PbI_3$ ($FA = CH(NH_2)_2^+$), δ-$CsPbI_3$, and δ-$CsSnI_3$.[2−6] These diverse metal-halide structures can host dramatically different electronic and optical properties, enabling not only the development of many engineered materials for applications such as high-performance photovoltaics and light-emitting devices[7,8] but also a promising platform for accessing novel electronic properties as seen in other low-dimensional materials.

Low-dimensional metal halides exhibit pronounced structural and electronic anisotropies.[9,10] Charge carriers are confined within 2D planes or 1D channels, significantly enhancing the quantum confinement and many-body effects.[11] These effects have induced anisotropic carrier transport and size/layer-dependent physical properties in systems such as halide perovskite nanowires,[12] and 2D perovskites,[1] providing an effective route for electronic structure modulation for potential optoelectronic applications. The anisotropic lattice structures of low-dimensional metal halides are also ideal candidates for synthesizing 1D conductive chains or 2D conductive films, which have long been of interest in both solid-state chemistry and condensed matter physics.[13,14] However, studies of the electronic anisotropy and potential novel electronic properties in these materials have been limited, partly because they typically have large band gaps and are insulating. Previous efforts to study these low-dimensional metal halides mainly focused on the syntheses of new compositions and fabrication of atomically thin films or nanowires at ambient pressure.[8,15−21]

Lattice compression has been used to effectively modify the electronic structures and improve the conductivity of halide perovskites.[22−31] Low-dimensional metal halides indeed attracted extensive attention in the high-pressure community in the past years.[32−44] These studies centered on tuning the materials' structural, electronic, and optical properties. So far, the electronic anisotropy in these materials has not been used

Received: October 13, 2022
Published: December 19, 2022

https://doi.org/10.1021/jacs.2c10884
J. Am. Chem. Soc. 2022, 144, 23595−23602

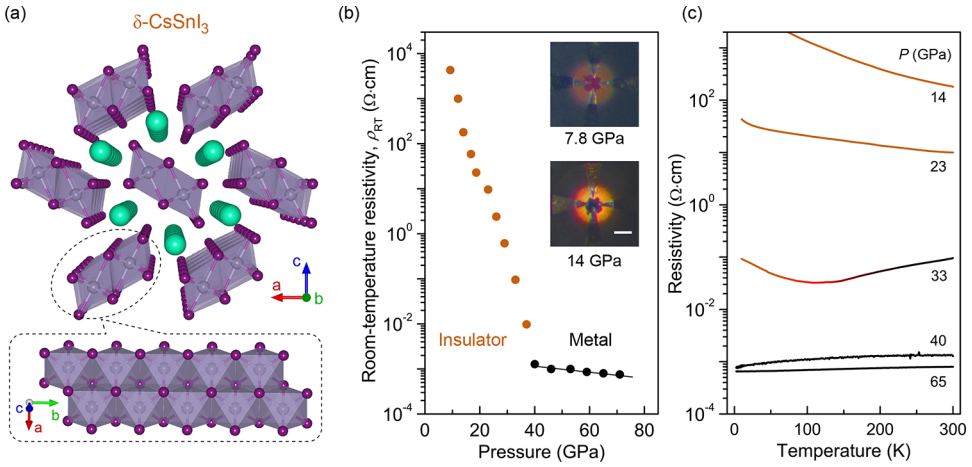

Figure 1. Resistivity of powdered δ-$CsSnI_3$ over a temperature range of 2−300 K and pressure up to 71 GPa. (a) Chain structure of δ-$CsSnI_3$ at ambient conditions with Cs (turquoise), Sn (gray), and I (purple) atoms shown. (b) Room-temperature resistivity (ρ_{RT}) as a function of pressure. Black line is a linear fit of the log ρ_{RT}−P curve above 40 GPa. Photomicrographs show the hand-wired electrode configuration for the resistivity measurements and the color change of the sample to opaque black under compression. Scale bar is 50 μm. (c) Resistivity−temperature (ρ−T) curves at representative pressures.

to realize intriguing electronic states, e.g., 1D metallicity. We recently reported that δ-$CsPbI_3$ transformed to a Fermi-liquid-like metal at high pressure as a result of Cs-mediated electron redistribution and electron−electron interaction; however, the structure concomitantly underwent a transition from the 1D chain structure to a 3D phase.[45]

In this work, we demonstrate that quasi-1D metallicity can be achieved in δ-$CsSnI_3$ at high pressure. Above 40 GPa, insulating δ-$CsSnI_3$ transforms to a metallic state while maintaining its 1D chain structure with edge-sharing octahedra. In contrast to ambient pressure where the Sn−Sn hybridization within the SnI_6 octahedral chain is negligible, calculations indicate that the Sn atoms hybridize significantly with each other in metallic δ-$CsSnI_3$, along with the enhancement of intrachain Sn−I coupling. The interactions between neighboring SnI_6 octahedral chains remain weak even above 40 GPa, resulting in a highly anisotropic electronic structure and quasi-1D metallicity.

2. EXPERIMENTAL DETAILS

2.1. Synthesis of δ-$CsSnI_3$ Samples. Yellow δ-$CsSnI_3$ samples were synthesized in a N_2-filled glovebox. Solid $SnCl_2$ (262.7 mg, 1.390 mmol) and CsI (361.1 mg, 1.390 mmol) powder precursors were dissolved in HI aq. (2 mL, 47 wt % in water, ~2.5% H_3PO_2) in two separate 4 mL vials. The two solutions were then mixed and stirred for 5 min. The resulting yellow solids were filtered using a fritted glass, transferred to a 20-mL vial, and heated at 40 °C under reduced pressure overnight. Needle-like single crystal samples were obtained with diameters and lengths of 1−10 μm and 50−500 μm, respectively. Portions of the samples were ground for 10 min with a mortar and pestle before loading for resistivity and X-ray diffraction (XRD) experiments. All the samples were stored, and all the experimental loadings were handled in an Ar-filled glovebox.

2.2. Resistivity Measurements. Low-temperature (2−300 K) resistivity measurements at high pressures were conducted in a physical property measurement system (PPMS DynaCool). A nonmagnetic diamond anvil cell (made from Be−Cu alloy) with beveled diamonds (inner/outer culet diameter of 100/300 μm) was used to apply the pressure. An insulating gasket was prepared by pressing a mixture of epoxy and cubic boron nitride powders (1:10 in weight) into a pre-indented rhenium gasket, as reported in our previous studies.[46,47] Four platinum foil electrodes were prepared on the insulating layer by a hand-wiring method. Pressure was calibrated at room temperature using the ruby fluorescence method (0.1−45 GPa)[48] and diamond Raman peaks (20−150 GPa).[49] No pressure-transmitting medium was used in the measurements to ensure good contact between the sample and the foil electrodes.

2.3. XRD Measurements. High-pressure XRD experiments were performed at Beamline 12.2.2 of the Advanced Light Source for runs 1 and 2 and HPCAT (16-BMD) of the Advanced Photon Source for run 3. The beam size used was about 10 μm × 10 μm at Beamline 12.2.2 and 4 μm × 4 μm at Beamline 16-BMD. A pair of 200-μm culet diamond anvils and a pre-indented tungsten gasket were used to generate and seal the pressure. An 80-μm hole was drilled in the center of the pre-indented tungsten gasket, serving as the sample chamber. Powdered δ-$CsSnI_3$ samples, pressure calibrants (a ruby ball of ~5 μm in diameter and a small piece of precompressed Au sheet), and a pressure-transmitting medium (silicone oil) were then loaded into the sample chamber in an Ar-filled glovebox.

2.4. Raman Measurements. Ultra-low frequency Raman spectra down to 10 cm^{-1} were collected using a Horiba LabRam HR Evolution Raman system at the Stanford Nano Shared Facilities (SNSF). A laser excitation wavelength of 633 nm was utilized. Raman spectra collected in the directions parallel and perpendicular to the SnI_6 octahedral chains were performed by rotating the diamond anvil cell using a rotation stage. Type-IIas diamonds were used to reduce the background. A small δ-$CsSnI_3$ single crystal with a needle-like shape (~10 μm in diameter and ~60 μm in length) was loaded, which helps identify the orientation of the sample for Raman measurements. Neon was used as the pressure-transmitting medium.

2.5. Density Functional Theory (DFT) Calculations. DFT with Perdew−Burke−Ernzerhof (PBE) exchange-correlation functional of generalized gradient approximation (GGA),[50] that is implemented in the Vienna ab initio simulation package (VASP),[51] was used in our calculations for structural optimization, band structures, density of states (DOS), and electron localization function of δ-$CsSnI_3$. The CASTEP mode was used to calculate the 3D orbital maps of the bands crossing the Fermi surface. A plane wave energy of 500 eV was set as the projector-augmented wave (PAW) pseudopotentials.[52] The valence electrons of Cs, Sn, and I atoms were $5s^25p^66s^1$, $4d^{10}5s^25p^2$, and $5s^25p^5$, respectively. A fine Monkhorst−Pack Brillouin zone sampling grid with a resolution of 0.02 × 2π $Å^{-1}$ was used in our calculations. The input structure at ambient pressure was from the ICSD (ICSD-14070). The theoretical structures at high pressure were obtained from the structural optimization calculations using the relaxed ambient structure as the initial configuration. The pressure was applied by setting the stress to a target value, which has been implemented in the VASP. At each pressure, atomic positions and

https://doi.org/10.1021/jacs.2c10884
J. Am. Chem. Soc. 2022, 144, 23595−23602

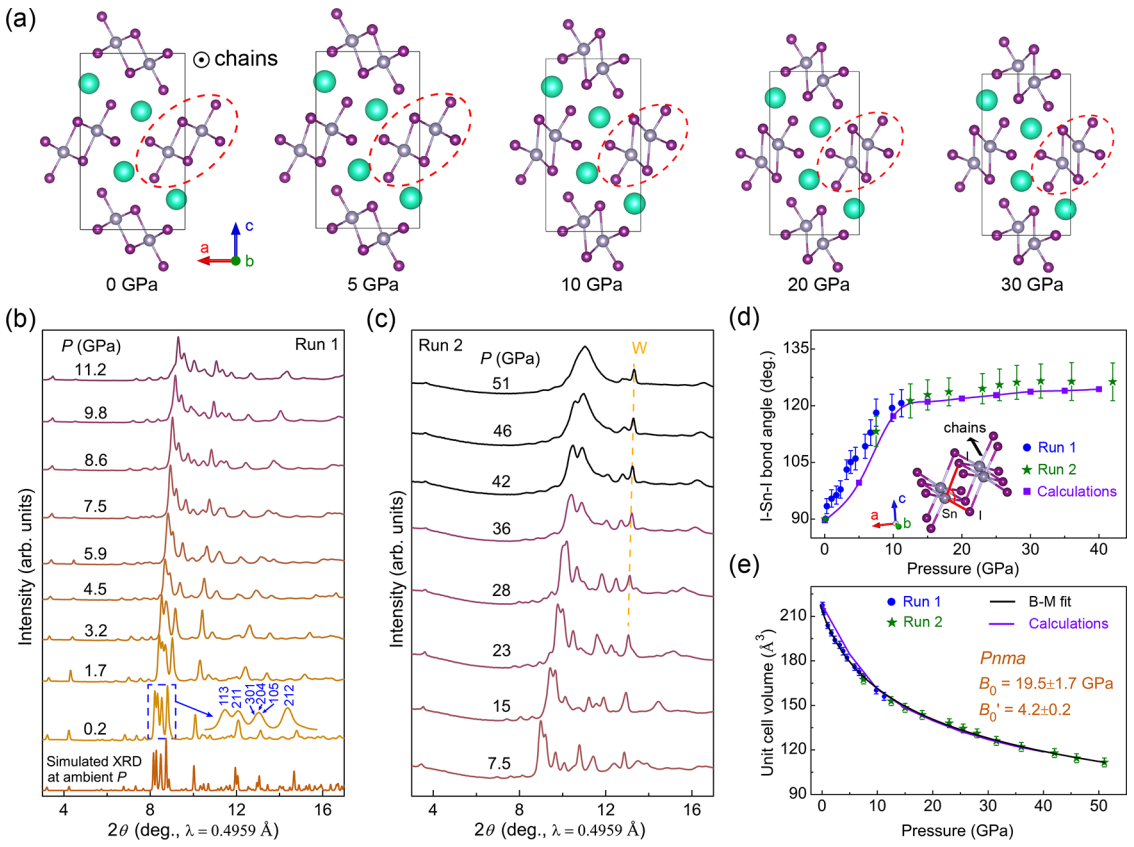

Figure 2. Structural evolution of δ-$CsSnI_3$ at high pressure. (a) Calculated structures of δ-$CsSnI_3$ at representative pressures showing the distortion of the SnI_6 octahedral chains under compression. The red dashed ellipses highlight the distortion of a SnI_6 octahedral chain as a function of pressure. (b) XRD patterns of powdered δ-$CsSnI_3$ in run 1. Pattern at the bottom is the simulated XRD at ambient pressure with a random distribution in the orientation of the crystallites. (c) XRD patterns of powdered δ-$CsSnI_3$ in run 2. Orange dashed line indicates the evolution of the diffraction peak from the tungsten (W) gasket. (d) Pressure dependence of the I−Sn−I bond angle obtained from Rietveld refinement of the XRD patterns in both experimental runs and calculations. (e) Pressure dependence of the unit cell volume. A fit to a third-order Birch−Murnaghan (B-M fit) equation of state is shown as a black solid line. The pressure interval for calculations is 5 GPa.

lattice parameters were relaxed until all the forces on the ions were <1 meV/Å. The relaxed lattice parameters are comparable with the experimental values obtained from the XRD experiments (see details in the Supporting Information).

3. RESULTS AND DISCUSSION

We measured the resistivity of δ-$CsSnI_3$ over a temperature range of 2−300 K at high pressure. The samples were loaded in an Ar-filled glovebox to avoid the oxidization of δ-$CsSnI_3$. At ambient pressure, the room-temperature resistivity (ρ_{RT}) of the wide-band gap insulator δ-$CsSnI_3$ (band gap ~2.6 eV[6]) is beyond the measurable range of the instrument. With increasing pressure, ρ_{RT} falls into the measurable range and is $\sim 4.3 \times 10^3$ Ω·cm at 9.2 GPa (Figure 1b), followed by a dramatic resistivity drop of seven orders of magnitude with further compression up to 40 GPa. The color of the sample changes from yellow to red and then to black. Above 40 GPa, log ρ_{RT} decreases linearly as a function of pressure at a rate of $-(5.4 \pm 0.2) \times 10^{-3}$ Ω·cm/GPa up to 71 GPa. The turning point shown in the $\rho_{RT} - P$ plot at 40 GPa suggests an electronic transition. During decompression, ρ_{RT} exceeds the measurable range again below 7.8 GPa, followed by the color of the sample going back to yellow.

The resistivity−temperature ($\rho-T$) curves at representative pressures confirm the electronic insulator-to-metal transition (Figure 1c). At pressures below 23 GPa, the slope of $\rho-T$ curves ($d\rho/dT$) is negative throughout the studied temperature range of 2−300 K, indicating insulating behavior. At a higher pressure of 33 GPa, $d\rho/dT$ is positive near room temperature but becomes negative below ~100 K. With further compression to 40 GPa, the sign reversal of $d\rho/dT$ is fully suppressed, and a positive $d\rho/dT$ is observed throughout 2−300 K, indicating a metallic state. The insulator-to-metal transition pressure (~40 GPa) is much lower than that of isostructural δ-$CsPbI_3$ (~80 GPa),[45] despite having similar band gaps at ambient conditions. In addition, in contrast to compressed $CsPbI_3$ where we found a Fermi-liquid-like state in the high-pressure metallic phase below 100 K,[45] no such behavior is observed in δ-$CsSnI_3$ up to 150 GPa (Figure S1).

We studied the structural evolution of δ-$CsSnI_3$ at high pressure using powder XRD. Three experimental runs were conducted where run 1 examined a low-pressure region (Figure 2b), and run 2 (Figure 2c) and run 3 (Figure S2) covered pressures above the insulator-to-metal transition. All the experimental results are self-consistent. At 0.2 GPa, δ-$CsSnI_3$ crystallizes in a *Pnma* structure with the lattice parameters of $a = 10.266 \pm 0.010$ Å, $b = 4.723 \pm 0.006$ Å, and $c = 17.575 \pm 0.015$ Å, consistent with the reported values at ambient conditions.[5] In this structure, the Sn atom is coordinated by six I atoms to form SnI_6 octahedra, which are edge-sharing to form a 1D SnI_6 double chain structure (Figure 1a) that is charge-balanced by the Cs cation. Although the

https://doi.org/10.1021/jacs.2c10884
J. Am. Chem. Soc. 2022, 144, 23595−23602

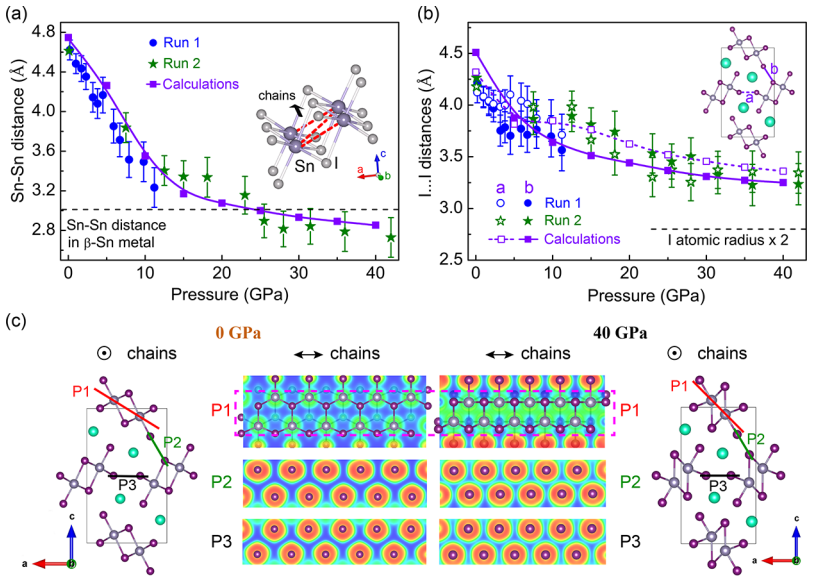

Figure 3. Intrachain Sn−Sn and interchain I...I distances and calculated electron localization function of δ-$CsSnI_3$ at representative pressures. (a) Sn−Sn distance in the SnI_6 octahedral chains (shown as the red dashed lines in the inset structure) as a function of pressure obtained from Rietveld refinement of the XRD patterns and calculations. Sn−Sn distance in β-Sn metal at ambient pressure reported in the ICSD (ICSD-106072) is shown as the dashed horizontal line for comparison. (b) Evolution of two I...I distances between neighboring SnI_6 octahedral chains (shown in the inset) determined from Rietveld refinement of the XRD patterns and calculations. (c) Electron localization function visualized on lattice planes P1, P2, and P3 at 0 and 40 GPa. P1 plane was set by choosing three Sn atoms in a SnI_6 octahedral chain to show the Sn−Sn hybridization. P2 and P3 planes were determined by three outer I atoms between neighboring chains to show the I...I interactions. Intrachain Sn−Sn hybridization (P1) is shown in the dashed magenta rectangle which clearly indicates that the Sn−Sn interaction develops at high pressure in the metallic phase.

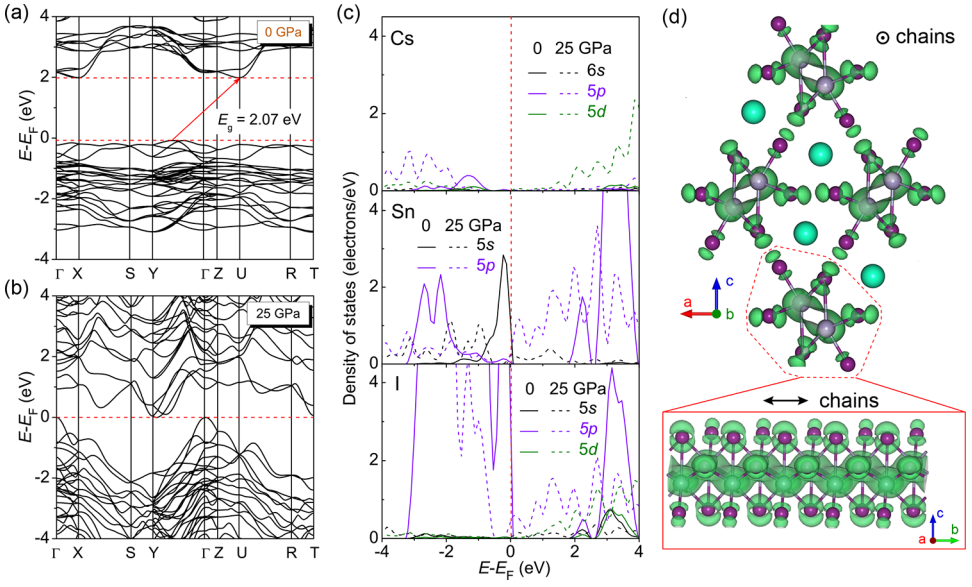

Figure 4. Electronic structure of δ-$CsSnI_3$ at representative pressures. Calculated band structures at (a) 0 GPa and (b) 25 GPa. (c) Calculated DOS at 0 (solid lines) and 25 GPa (dashed lines). (d) 3D orbital maps of the bands crossing the Fermi level at 25 GPa showing the quasi-1D conductive SnI_6 octahedral chains. Iso-surface value is set to be 0.01 e/au.

octahedra distort, the *Pnma* chain structure is maintained at pressures above 40 GPa where δ-$CsSnI_3$ becomes metallic. No additional diffraction peaks appear during the compression process, although there is an overlap of some of the reflections such as the strongest (113), (211), and (212) peaks (Figure 2b,c).

The relative intensities of the diffraction peaks, especially the strongest (113), (211), and (212) reflections, evolve continuously as a function of pressure, indicating that the atomic positions change, and the internal chain structure is being distorted while the *Pnma* symmetry remains. At 0.2 GPa, the (212) peak is the strongest, and its intensity decreases dramatically with pressure. Above 3.2 GPa, the (113) reflection becomes the most intense peak, and its relative intensity keeps changing with further compression. The peak intensities of the 0.2-GPa pattern are consistent with the simulated XRD pattern at ambient pressure with a random distribution in the orientation of the crystallites. At high pressure, smooth diffraction rings were collected and no preferred orientation-induced enhancement in the intensities of a set of parallel

https://doi.org/10.1021/jacs.2c10884
J. Am. Chem. Soc. 2022, 144, 23595−23602

lattice planes was observed, indicating that the intensity changes in compressed δ-$CsSnI_3$ are not caused by the texture or the orientation effect. To quantitatively analyze the structural evolution as a function of pressure, we performed Rietveld refinement on the XRD patterns using the GSAS-II software package.[53] The fitted patterns without applying the preferred orientation match well with the experimental ones (Figure S3). The refinement results show that the I−Sn−I bond angle (the red dashed ellipses in Figure 2a and the inset of Figure 2d) within the SnI_6 octahedral chain increases sharply with pressure (Figure 2d), a clear indication that the chains are heavily distorted. Structural optimization results obtained from first-principles DFT calculations are comparable with the experimental values (Figure 2d,e).

The structural evolution of δ-$CsSnI_3$ is considerably different from that of isostructural δ-$CsPbI_3$ under compression. While δ-$CsPbI_3$ goes through a sequence of Pb−I bond rearrangements within the PbI_6 octahedral chains and new bond formation between neighboring chains to crystallize in a 3D $Pmn2_1$ structure,[45] δ-$CsSnI_3$ solely distorts the SnI_6 octahedral chains and stays in the 1D structure under compression. The Sn atom remains coordinated by six I anions (Figure S4). These distinct structural transitions may in part be due to the atomic radius difference between the Sn and Pb atoms. The lower critical pressure for the insulator-to-metal transition in δ-$CsSnI_3$ compared to that of δ-$CsPbI_3$ may be a result of the different structural evolution and metal-halide coordination changes under compression, and the softer lattice of δ-$CsSnI_3$ (bulk modulus B_0 = 19.5 ± 1.7 GPa, Figure 2e) with a larger V_0/V at the same pressure applied compared to δ-$CsPbI_3$ (B_0 = 22.1 ± 1.2 GPa). Furthermore, the newly formed Sn−Sn interaction and enhanced orbital overlap in the Sn−I bonds that we discuss in the following section (Figure 3) may also contribute to the much decreased metallization pressure in δ-$CsSnI_3$, since the Sn-5p state makes dominant contributions to the electronic bands crossing the Fermi level that increases the density of states near the Fermi surface (Figure 4).

We extracted the Sn−Sn distance (Figure 3a) and Sn−I bond lengths (Figure S5) in the SnI_6 octahedral chains and the I...I distances between neighboring chains (Figure 3b) from Rietveld refinement of the XRD patterns. The values are in good agreement with those obtained from optimized structures by DFT calculations. We find that the intrachain and interchain interactions are highly anisotropic. The Sn−Sn distance decreases sharply as a function of pressure. Above 25 GPa, the distance becomes comparable with the Sn−Sn distance in metallic β-Sn at ambient pressure (Figure 3a). The intrachain Sn−I bond lengths also reduce with pressure (Figure S5). On the other hand, although the interchain I...I distances decrease appreciably with increasing pressure (Figure 3b), at 40 GPa, the two shortest distances, i.e., 3.261 and 3.372 Å, are still far away from twice the atomic radius (~2.8 Å) of I,[54] or the I−I bond length (2.715 Å) in solid molecular I_2.[55] Previous studies indicated that solid I_2 became a molecular metal at 16−22 GPa.[56−59] The intermolecular I...I distances relevant for the metallic transition in I_2 reduced to 2.95−3.05 Å, which were much shorter than the interchain I...I distances in metallic δ-$CsSnI_3$ at 40 GPa. This implies that the interchain I...I interactions are weak and not responsible for the metallicity of 1D δ-$CsSnI_3$. The anisotropy in 1D δ-$CsSnI_3$ resembles that in 2D materials, that is, strong interactions within the 2D layers (or 1D SnI_6 octahedral chains) but weak coupling between adjacent 2D layers (or 1D SnI_6 octahedral chains).

Raman spectroscopy measurements on a δ-$CsSnI_3$ single crystal confirm the stability of the chain structure and the anisotropic behavior under compression. At the starting pressure of 1.5 GPa, the Raman spectra (Figure S6) are similar with isostructural δ-$CsPbI_3$.[60] With further compression, there are some changes in the relative intensities and overlap of some vibrational modes, but no additional Raman modes appear and all peaks blueshift, indicating that no structural transition occurs in 1D δ-$CsSnI_3$ under compression. The peaks in the Raman spectra collected along the chain direction (// b-axis) disappear at ~30.7 GPa, which coincides with the onset pressure of the metallic transition (~33 GPa). In contrast, the Raman modes in the spectra collected perpendicular to the chain direction (⊥ b-axis) remain visible up to ~40 GPa, corroborating the anisotropic behavior of the material. The flat Raman spectra beyond 40 GPa are consistent with the metallization of 1D δ-$CsSnI_3$.

Electron localization function calculations also support the highly anisotropic interactions within versus between the SnI_6 octahedral chains. We selected four representative lattice planes (P1, P2, and P3 in Figure 3c, P4 in Figure S7) to study the electron localization of δ-$CsSnI_3$ at 0 and 40 GPa. At 0 GPa, the Sn−I hybridization within the SnI_6 octahedral chains is strong (P4), and the valence electrons are mostly localized around the Sn−I bonds. The intrachain Sn−Sn hybridization (P1) and interchain I...I interactions (P2 and P3) are negligible. However, pronounced changes occur at 40 GPa. The intrachain Sn atoms hybridize significantly (P1), and valence electrons become increasingly delocalized among the Sn atoms (the green channel along the Sn atoms in P1 at 40 GPa). The valence electrons around the Sn−I bonds also show pronounced delocalization (P4 in Figure S7). In contrast, the I...I hybridization between neighboring SnI_6 octahedral chains remains weak (P2 and P3). The interaction anisotropy is consistent with the intrachain Sn−Sn and Sn−I, and interchain I...I distances discussed above (Figure 3a,b).

Electronic structure calculations further indicate that interaction anisotropy in δ-$CsSnI_3$ induces a highly anisotropic electronic structure and quasi-1D metallicity. Band structure calculations indicate that at 0 GPa, δ-$CsSnI_3$ has an indirect band gap of 2.07 eV (~0.5 eV smaller than the experimental value[6]) with the conduction band minimum (CBM) and the valence band maximum (VBM) located at the high-symmetry U point and along the Γ−Y direction (Figures 4a, and S8 and S9), respectively. The VBM and the CBM are mainly composed of the Sn-5s and I-5p states, and the Sn-5p and I-5p states, respectively (Figure 4c). With applying pressure, the band gap of δ-$CsSnI_3$ reduces and finally closes at 25 GPa (Figure 4b) with the VBM and the CBM located at the Γ point and along the Γ−Y direction, respectively. After accounting for the band gap underestimation from the GGA used in our calculations (see Figure S10 for details about the band gap correction), a critical pressure of ~33 GPa is estimated for the metallic transition, which is in excellent agreement with the value obtained from our resistivity measurements. The DOS results at 25 GPa (Figure 4c) reveal that the closure of the band gap is caused by the significant hybridization of I-5p and Sn-5p states. Importantly, the Sn-5p orbital has a much larger contribution to the states near the Fermi surface compared to the I-5p orbital, which indicates that, in addition to the enhanced intrachain Sn−I coupling, the pressure-induced

https://doi.org/10.1021/jacs.2c10884
J. Am. Chem. Soc. 2022, 144, 23595−23602

formation of intrachain Sn−Sn hybridization also plays a sizable role in the orbital states near the Fermi surface, consistent with the electron localization function calculations. The formation of intrachain Sn−Sn coupling and the enhancement of Sn−I hybridization eventually drive the metallic transition of the SnI_6 octahedral chains. Similar metal−metal interactions have been invoked in the pressure-induced metallization of 3D $(CH_3NH_3)PbI_3$ studied by DFT calculations.[61] On the other hand, the weak interchain I...I interactions in δ-$CsSnI_3$ restrain free electrons from moving between neighboring chains. The combined effect enables a quasi-1D metallic state in δ-$CsSnI_3$.

Such quasi-1D metallicity can also be clearly observed from the 3D orbital maps of the electronic bands crossing the Fermi level (Figure 4d). These are the bands that mainly influence the electrical properties of the material. The Sn-5*p* and I-5*p* bands crossing the Fermi level form a zigzag-shaped pattern along the crystallographic chain direction (*b*-axis), while the orbital overlap between neighboring SnI_6 octahedral chains is minimal, resulting in a quasi-1D Fermi surface and consequently quasi-1D metallicity in δ-$CsSnI_3$ under compression. We notice that the Cs-5*d* and I-5*d* orbitals have very limited contribution to the DOS near the Fermi surface, although they broaden and contribute to the conduction band 1 eV above the Fermi surface. Therefore, their effects on the electrical transport are negligible in compressed δ-$CsSnI_3$. This in part explains the different low-temperature electrical transport behavior between δ-$CsSnI_3$ and δ-$CsPbI_3$ under compression. In metallic δ-$CsSnI_3$, no Fermi liquid-like state is observed due to the lack of *d*-orbital contributions and related electron−electron interactions.

4. CONCLUSIONS

Quasi-1D metallicity was demonstrated by compressing δ-$CsSnI_3$ to above 40 GPa. The chain structure of δ-$CsSnI_3$, despite substantial intrachain distortion, is maintained in the high-pressure metallic phase. Pressure induces Sn−Sn hybridization and enhances Sn−I coupling within the chain, which leads to the broadening of the valence and conduction bands, closure of the band gap, and formation of 1D conductive SnI_6 octahedral chains. On the other hand, the interchain I...I interactions remain insignificant at high pressure which prohibits electron mobility between adjacent chains. Similar low-dimensional metallicity could be widely attainable in other 2D and 1D metal halides. As observed in 2D materials where reduced electronic dimensionality typically associates with special topology of the Fermi surface and intriguing electronic transitions, our study opens a high-pressure route for achieving the rich electronic phenomena that 2D and 1D metal halides have to offer.

■ ASSOCIATED CONTENT

Supporting Information

The Supporting Information is available free of charge at https://pubs.acs.org/doi/10.1021/jacs.2c10884.

Fitting of the $\rho-T$ curves with different models; XRD patterns of powdered δ-$CsSnI_3$ under compression run 3; Rietveld refinement of XRD patterns at selected pressures; structural models of δ-$CsSnI_3$; Sn−I bond lengths in the SnI_6 double chains as a function of pressure; crystallographic orientation-dependent Raman spectra of a $CsSnI_3$ single crystal at high pressure; electron localization function presented on the lattice plane P4; high-symmetry points in the first Brillouin zone of δ-$CsSnI_3$; evolution of the highest valence band and the lowest conduction band as a function of pressure; calculated band gap of δ-$CsSnI_3$ as a function of pressure; lattice parameters of δ-$CsSnI_3$ as a function of pressure; and detailed structural information for δ-$CsSnI_3$ with the *Pnma* symmetry at selected pressures (PDF)

■ AUTHOR INFORMATION

Corresponding Authors

Ketao Yin − *School of Physics and Electronic Engineering, Linyi University, Linyi, Shandong 276005, China;* orcid.org/0000-0002-6179-3409; Email: yinketao@lyu.edu.cn

Yu Lin − *Stanford Institute for Materials and Energy Sciences, SLAC National Accelerator Laboratory, Menlo Park, California 94025, United States;* orcid.org/0000-0001-5174-9546; Email: lyforest@stanford.edu

Authors

Feng Ke − *Stanford Institute for Materials and Energy Sciences, SLAC National Accelerator Laboratory, Menlo Park, California 94025, United States; Department of Geological Sciences, Stanford University, Stanford, California 94305, United States; State Key Laboratory of Metastable Materials Science and Technology, Yanshan University, Qinhuangdao, Hebei 066004, China;* orcid.org/0000-0002-1906-9636

Jiejuan Yan − *Department of Geological Sciences, Stanford University, Stanford, California 94305, United States;* orcid.org/0000-0002-3286-5020

Roc Matheu − *Department of Chemistry, Stanford University, Stanford, California 94305, United States;* Present Address: Departament de Química Inorgànica i Orgànica, Institut de Recerca de Química Teòrica i Computacional, Universitat de Barcelona, Diagonal 645, 08028 Barcelona, Spain. (R.M.)

Shanyuan Niu − *National Laboratory of Solid State Microstructures, College of Engineering and Applied Sciences, Nanjing University, Nanjing, Jiangsu 210093, China*

Nathan R. Wolf − *Department of Chemistry, Stanford University, Stanford, California 94305, United States*

Hong Yang − *Department of Geological Sciences, Stanford University, Stanford, California 94305, United States*

Jiajia Wen − *Stanford Institute for Materials and Energy Sciences, SLAC National Accelerator Laboratory, Menlo Park, California 94025, United States;* orcid.org/0000-0002-1651-3578

Young S. Lee − *Stanford Institute for Materials and Energy Sciences, SLAC National Accelerator Laboratory, Menlo Park, California 94025, United States; Department of Applied Physics, Stanford University, Stanford, California 94305, United States*

Hemamala I. Karunadasa − *Stanford Institute for Materials and Energy Sciences, SLAC National Accelerator Laboratory, Menlo Park, California 94025, United States; Department of Chemistry, Stanford University, Stanford, California 94305, United States;* orcid.org/0000-0003-4949-8068

Wendy L. Mao − *Stanford Institute for Materials and Energy Sciences, SLAC National Accelerator Laboratory, Menlo Park, California 94025, United States; Department of*

Geological Sciences, Stanford University, Stanford, California 94305, United States

Complete contact information is available at: https://pubs.acs.org/10.1021/jacs.2c10884

Notes

The authors declare no competing financial interest.

■ ACKNOWLEDGMENTS

This work was supported by the Department of Energy (DOE), Office of Science, Basic Energy Sciences, Materials Sciences and Engineering Division (DE-AC02-76SF00515). Portions of this work were performed at Beamline 12.2.2, Advanced Light Source (ALS), Lawrence Berkeley National Laboratory, and HPCAT (Sector 16), Advanced Photon Source (APS), Argonne National Laboratory (ANL). Beamline 12.2.2 is a DOE Office of Science User Facility under Contract No. DE-AC02-05CH11231. HPCAT operations are supported by DOE-NNSA's Office of Experimental Sciences. The APS is a DOE Office of Science User Facility operated for the DOE Office of Science by ANL under Contract No. DE-AC02-06CH11357. Part of this work was performed at the Stanford Nano Shared Facilities (SNSF), supported by the National Science Foundation under award ECCS-2026822. The simulation work by K.Y. was supported by the Natural Science Foundation of China under Grant No. 11904148.

■ REFERENCES

(1) Mitzi, D. B. Synthesis, structure, and properties of organic-inorganic perovskites and related Materials. In *Progress in Inorganic Chemistry*; Karlin, K. D., Ed.; Wiley, 1999; Vol. *48*, pp 1−121.

(2) Stoumpos, C. C.; Malliakas, C. D.; Kanatzidis, M. G. Semiconducting tin and lead iodide perovskites with organic cations: Phase transitions, high mobilities, and near-infrared photoluminescent properties. *Inorg. Chem.* **2013**, *52*, 9019−9038.

(3) Trots, D. M.; Myagkota, S. V. High-temperature structural evolution of caesium and rubidium triiodoplumbates. *J. Phys. Chem. Solids* **2008**, *69*, 2520−2526.

(4) Straus, D. B.; Guo, S.; Cava, R. J. Kinetically stable single crystals of perovskite-phase $CsPbI_3$. *J. Am. Chem. Soc.* **2019**, *141*, 11435−11439.

(5) Mauersberger, P.; Huber, F. Structure of caesium triiodostannate(II). *Acta Cryst.* **1980**, *B36*, 683−684.

(6) Chung, I.; Song, J.-H.; Im, J.; Androulakis, J.; Malliakas, C. D.; Li, H.; Freeman, A. J.; Kenney, J. T.; Kanatzidis, M. G. $CsSnI_3$: semiconductor or metal? High electrical conductivity and strong near-infrared photoluminescence from a single material. High hole mobility and phase-transitions. *J. Am. Chem. Soc.* **2012**, *134*, 8579−8587.

(7) Kojima, A.; Teshima, K.; Shirai, Y.; Miyasaka, T. Organometal halide perovskites as visible-light sensitizers for photovoltaic cells. *J. Am. Chem. Soc.* **2009**, *131*, 6050−6051.

(8) Smith, M. D.; Connor, B. A.; Karunadasa, H. I. Tuning the luminescence of layered halide perovskites. *Chem. Rev.* **2019**, *119*, 3104−3139.

(9) Fang, C.; Xu, M.; Ma, J.; Wang, J.; Jin, L.; Xu, M.; Li, D. Large optical anisotropy in two-dimensional perovskite $[CH(NH_2)_2][C(NH_2)_3]PbI_4$ with corrugated inorganic layers. *Nano Lett.* **2020**, *20*, 2339−2347.

(10) Zhao, J.; Zhao, Y.; Guo, Y.; Zhan, X.; Feng, J.; Geng, Y.; Yuan, M.; Fan, X.; Gao, H.; Jiang, L.; Yan, Y.; Wu, Y. Layered metal-halide perovskite single-crystalline microwire arrays for anisotropic nonlinear optics. *Adv. Funct. Mater.* **2021**, *31*, No. 2105855.

(11) Blancon, J.-C.; Tsai, H.; Nie, W.; Stoumpos, C. C.; Pedesseau, L.; Katan, C.; Kepenekian, M.; Soe, C. M. M.; Appavoo, K.; Sfeir, M. Y.; Tretiak, S.; Ajayan, P. M.; Kanatzidis, M. G.; Even, J.; Crochet, J. J.; Mohite, A. D. Extremely efficient internal exciton dissociation through edge states in layered 2D perovskites. *Science* **2017**, *355*, 1288−1292.

(12) Oksenberg, E.; Merdasa, A.; Houben, L.; Kaplan-Ashiri, I.; Rothman, A.; Scheblykin, I. G.; Unger, E. L.; Joselevich, E. Large lattice distortions and size-dependent bandgap modulation in epitaxial halide perovskite nanowires. *Nat. Commun.* **2020**, *11*, 489.

(13) Campbell, M. G.; Powers, D. C.; Raynaud, J.; Graham, M. J.; Xie, P.; Lee, E.; Ritter, T. Synthesis and structure of solution-stable one-dimensional palladium wires. *Nat. Chem.* **2011**, *3*, 949−953.

(14) Li, X.; Lv, H.; Dai, J.; Ma, L.; Zeng, X. C.; Wu, X.; Yang, J. Half-metallicity in one-dimensional metal trihydride molecular nanowires. *J. Am. Chem. Soc.* **2017**, *139*, 6290−6293.

(15) Gangadharan, D. T.; Ma, D. Searching for stability at lower dimensions: current trends and future prospects of layered perovskite solar cells. *Energy Environ. Sci.* **2019**, *12*, 2860−2889.

(16) Ricciardulli, A. G.; Yang, S.; Smet, J. H.; Saliba, M. Emerging perovskite monolayers. *Nat. Mater.* **2021**, *20*, 1325−1336.

(17) Tsai, H.; Nie, W.; Blancon, J.-C.; Stoumpos, C. C.; Asadpour, R.; Harutyunyan, B.; Neukirch, A. J.; Verduzco, R.; Crochet, J. J.; Tretiak, S.; Pedesseau, L.; Even, J.; Alam, M. A.; Gupta, G.; Lou, J.; Ajayan, P. M.; Bedzyk, M. J.; Kanatzidis, M. G.; Mohite, A. D. High-efficiency two-dimensional Ruddlesden−Popper perovskite solar cells. *Nature* **2016**, *536*, 312−316.

(18) Dou, L.; Wong, A. B.; Yu, Y.; Lai, M.; Kornienko, N.; Eaton, S. W.; Fu, A.; Bischak, C. G.; Ma, J.; Ding, T.; Ginsberg, N. S.; Wang, L.-W.; Alivisatos, A. P.; Yang, P. Atomically thin two-dimensional organic-inorganic hybrid perovskites. *Science* **2015**, *349*, 1518−1521.

(19) Mao, L.; Stoumpos, C. C.; Kanatzidis, M. G. Two-dimensional hybrid halide perovskites: principles and promises. *J. Am. Chem. Soc.* **2019**, *141*, 1171−1190.

(20) Shi, E.; Yuan, B.; Shiring, S. B.; Gao, Y.; Akriti; Guo, Y.; Su, C.; Lai, M.; Yang, P.; Kong, J.; Savoie, B. M.; Yu, Y.; Dou, L. Two-dimensional halide perovskite lateral epitaxial heterostructures. *Nature* **2020**, *580*, 614−620.

(21) Blancon, J.-C.; Even, J.; Stoumpos, C. C.; Kanatzidis, M. G.; Mohite, A. D. Semiconductor physics of organic−inorganic 2D halide perovskites. *Nat. Nanotechnol.* **2020**, *15*, 969−985.

(22) Lü, X.; Wang, Y.; Stoumpos, C. C.; Hu, Q.; Guo, X.; Chen, H.; Yang, L.; Smith, J. S.; Yang, W.; Zhao, Y.; Xu, H.; Kanatzidis, M. G.; Jia, Q. Enhanced structural stability and photo responsiveness of $CH_3NH_3SnI_3$ perovskite via pressure-induced amorphization and recrystallization. *Adv. Mater.* **2016**, *28*, 8663−8668.

(23) Jaffe, A.; Lin, Y.; Beavers, C. M.; Voss, J.; Mao, W. L.; Karunadasa, H. I. High-pressure single-crystal structures of 3D lead-halide hybrid perovskites and pressure effects on their electronic and optical properties. *ACS Cent. Sci.* **2016**, *2*, 201−209.

(24) Jaffe, A.; Lin, Y.; Karunadasa, H. I. Halide perovskites under pressure: accessing new properties through lattice compression. *ACS Energy Lett.* **2017**, *2*, 1549−1555.

(25) Beimborn, J. C.; Hall, L. M. G.; Tongying, P.; Dukovic, G.; Weber, J. M. Pressure response of photoluminescence in cesium lead iodide perovskite nanocrystals. *J. Phys. Chem. C* **2018**, *122*, 11024−11030.

(26) Wang, Y.; Lü, X.; Yang, W.; Wen, T.; Yang, L.; Ren, X.; Wang, L.; Lin, Z.; Zhao, Y. Pressure-induced phase transformation, reversible amorphization, and anomalous visible light response in organolead bromide perovskite. *J. Am. Chem. Soc.* **2015**, *137*, 11144−11149.

(27) Yesudhas, S.; Morrell, M. V.; Anderson, M. J.; Ullrich, C. A.; Kenney-Benson, C.; Xing, Y.; Guha, S. Pressure-induced phase changes in cesium lead bromide perovskite nanocrystals with and without Ruddlesden−Popper faults. *Chem. Mater.* **2020**, *32*, 785−794.

(28) Liu, G.; Kong, L.; Gong, J.; Yang, W.; Mao, H.-K.; Hu, Q.; Liu, Z.; Schaller, R. D.; Zhang, D.; Xu, T. Pressure-induced bandgap optimization in lead-based perovskites with prolonged carrier lifetime and ambient retainability. *Adv. Funct. Mater.* **2017**, *27*, No. 1604208.

(29) Matheu, R.; Ke, F.; Breidenbach, A.; Wolf, N.; Lee, Y.; Liu, Z.; Leppert, L.; Lin, Y.; Karunadasa, H. Charge reservoirs in an expanded halide perovskite analog: enhancing high-pressure conductivity

through redox-active molecules. *Angew. Chem., Int. Ed.* **2022**, *61*, No. e202202911.
(30) Kong, L.; Liu, G.; Gong, J.; Mao, L.; Chen, M.; Hu, Q.; Lü, X.; Yang, W.; Kanatzidis, M. G.; Mao, H.-k. Highly tunable properties in pressure-treated two-dimensional Dion-Jacobson perovskites. *Proc. Natl. Acad. Sci. U. S. A.* **2020**, *117*, 16121−16126.
(31) Jaffe, A.; Lin, Y.; Mao, W. L.; Karunadasa, H. I. Pressure-induced metallization of the halide perovskite $(CH_3NH_3)PbI_3$. *J. Am. Chem. Soc.* **2017**, *139*, 4330−4333.
(32) Liang, Y.; Huang, X.; Huang, Y.; Wang, X.; Li, F.; Wang, Y.; Tian, F.; Liu, B.; Shen, Z. X.; Cui, T. New metallic ordered phase of perovskite $CsPbI_3$ under pressure. *Adv. Sci.* **2019**, *6*, No. 1900399.
(33) Wang, P.; Guan, J.; Galeschuk, D. T. K.; Yao, Y.; He, C. F.; Jiang, S.; Zhang, S.; Liu, Y.; Jin, M.; Jin, C.; Song, Y. Pressure-induced polymorphic, optical, and electronic transitions of formamidinium lead iodide perovskite. *J. Phys. Chem. Lett.* **2017**, *8*, 2119−2125.
(34) Liu, G.; Gong, J.; Kong, L.; Schaller, R. D.; Hu, Q.; Liu, Z.; Yan, S.; Yang, W.; Stoumpos, C. C.; Kanatzidis, M. G.; Mao, H.-K.; Xu, T. Isothermal pressure-derived metastable states in 2D hybrid perovskites showing enduring bandgap narrowing. *Proc. Natl. Acad. Sci. U. S. A.* **2018**, *115*, 8076−8081.
(35) Fang, Y.; Zhang, L.; Wu, L.; Yan, J.; Lin, Y.; Wang, K.; Mao, W. L.; Zou, B. Pressure-induced emission (PIE) and phase transition of a two-dimensional halide double perovskite $(BA)_4AgBiBr_8$ (BA = $CH_3(CH_2)_3NH_3^+$). *Angew. Chem., Int. Ed.* **2019**, *58*, 15249−15253.
(36) Shi, Y.; Ma, Z.; Zhao, D.; Chen, Y.; Cao, Y.; Wang, K.; Xiao, G.; Zou, B. Pressure-induced emission (PIE) of one-dimensional organic tin bromide perovskites. *J. Am. Chem. Soc.* **2019**, *141*, 6504−6508.
(37) Yin, T.; Liu, B.; Yan, J.; Fang, Y.; Chen, M.; Chong, W. K.; Jiang, S.; Kuo, J.-L.; Fang, J.; Liang, P.; Wei, S.; Loh, K. P.; Sum, T. C.; White, T. J.; Shen, Z. X. Pressure-engineered structural and optical properties of two-dimensional $(C_4H_9NH_3)_2PbI_4$ perovskite exfoliated nm-thin flakes. *J. Am. Chem. Soc.* **2019**, *141*, 1235−1241.
(38) Liu, G.; Kong, L.; Guo, P.; Stoumpos, C. C.; Hu, Q.; Liu, Z.; Cai, Z.; Gosztola, D. J.; Mao, H.-K.; Kanatzidis, M. G.; Schaller, R. D. Two regimes of bandgap red shift and partial ambient retention in pressure-treated two-dimensional perovskites. *ACS Energy Lett.* **2017**, *2*, 2518−2524.
(39) Guo, S.; Zhao, Y.; Bu, K.; Fu, Y.; Luo, H.; Chen, M.; Hautzinger, M. P.; Wang, Y.; Jin, S.; Yang, W.; Lv, X. Pressure-suppressed carrier trapping leads to enhanced emission in two-dimensional perovskite $(HA)_2(GA)Pb_2I_7$. *Angew. Chem., Int. Ed.* **2020**, *59*, 17533−17539.
(40) Liang, Y.; Wu, M.; Tian, C.; Huang, X.; Huang, Y.; Lekina, Y.; Shen, Z. X.; Yang, X. Pressure-tuned quantum well configuration in two-dimensional $PA_8Pb_5I_{18}$ perovskites for highly efficient yellow fluorescence. *ACS Appl. Energy Mater.* **2021**, *4*, 10003−10011.
(41) Zhang, L.; Wang, K.; Lin, Y.; Zou, B. Pressure effects on the electronic and optical Properties in low-dimensional metal halide perovskites. *J. Phys. Chem. Lett.* **2020**, *11*, 4693−4701.
(42) Umeyama, D.; Lin, Y.; Karunadasa, H. I. Red-to-black piezochromism in a compressible Pb−I−SCN layered perovskite. *Chem. Mater.* **2016**, *28*, 3241−3244.
(43) Jaffe, A.; Lin, Y.; Mao, W. L.; Karunadasa, H. I. Pressure-induced conductivity and yellow-to-black piezochromism in a layered Cu−Cl hybrid perovskite. *J. Am. Chem. Soc.* **2015**, *137*, 1673−1678.
(44) Jaffe, A.; Mack, S. A.; Lin, Y.; Mao, W. L.; Neaton, J. B.; Karunadasa, H. I. High compression-induced conductivity in a layered Cu-Br perovskite. *Angew. Chem., Int. Ed.* **2020**, *132*, 4046−4051.
(45) Ke, F.; Yan, J.; Niu, S.; Wen, J.; Yin, K.; Yang, H.; Wolf, N. R.; Tzeng, Y.-K.; Karunadasa, H. I.; Lee, Y. S.; Mao, W. L.; Lin, Y. Cesium-mediated electron redistribution and electron-electron interaction in high-pressure metallic $CsPbI_3$. *Nat. Commun.* **2022**, *13*, 7067.
(46) Ke, F.; Dong, H.; Chen, Y.; Zhang, J.; Liu, C.; Zhang, J.; Gan, Y.; Han, Y.; Chen, Z.; Gao, C.; Wen, J.; Yang, W.; Chen, X.-J.; Struzhkin, V. V.; Mao, H.-k.; Chen, B. Decompression-driven superconductivity enhancement in In_2Se_3. *Adv. Mater.* **2017**, *29*, No. 1701983.
(47) Ke, F.; Chen, Y.; Yin, K.; Yan, J.; Zhang, H.; Liu, Z.; Tse, J. S.; Wu, J.; Mao, H.-K.; Chen, B. Large bandgap of pressurized trilayer graphene. *Proc. Natl. Acad. Sci. U. S. A.* **2019**, *116*, 9186−9190.
(48) Mao, H.; Xu, J.-A.; Bell, P. Calibration of the ruby pressure gauge to 800 kbar under quasi-hydrostatic conditions. *J. Geophys. Res. Solid Earth* **1986**, *91*, 4673−4676.
(49) Akahama, Y.; Kawamura, H. Pressure calibration of diamond anvil Raman gauge to 310 GPa. *J. Appl. Phys.* **2006**, *100*, No. 043516.
(50) Shi, J. M.; Peeters, F. M.; Hai, G. Q.; Devreese, J. T. Erratum: Donor transition energy in GaAs superlattices in a magnetic field along the growth axis. *Phys. Rev. B* **1993**, *48*, 4978−4978.
(51) Kresse, G.; Furthmüller, J. Efficient iterative schemes for ab initio total-energy calculations using a plane-wave basis set. *Phys. Rev. B* **1996**, *54*, 11169−11186.
(52) Bliichl, P. E. Projector augmented-wave method. *Phys. Rev. B* **1994**, *50*, 17953−17979.
(53) Toby, B. H.; Von Dreele, R. B. GSAS-II: the genesis of a modern open-source all purpose crystallography software package. *J. Appl. Crystallogr.* **2013**, *46*, 544−549.
(54) Slater, J. C. Atomic radii in crystals. *J. Chem. Phys.* **1964**, *41*, 3199−3204.
(55) Van Bolhuis, F.; Koster, P. B.; Migchelsen, T. Refinement of the crystal structure of iodine at 110° K. *Acta Cryst.* **1967**, *23*, 90−91.
(56) Riggleman, B. M.; Drickamer, H. G. Approach to the metallic state as obtained from optical and electrical measurements. *J. Chem. Phys.* **1963**, *38*, 2721−2724.
(57) Shimomura, C.; Takemura, K.; Fujii, Y.; Minomura, S.; Mori, M.; Noda, Y.; Yamada, Y. Structure analysis of high-pressure metallic state of iodine. *Phys. Rev. B* **1978**, *18*, 715−719.
(58) Sakai, N.; Takemura, K.-I.; Tsuji, K. Electrical properties of high-pressure metallic modification of iodine. *J. Phys. Soc. Jpn.* **1982**, *51*, 1811−1816.
(59) Kenichi, T.; Kyoko, S.; Hiroshi, F.; Mitsuko, O. Modulated structure of solid iodine during its molecular dissociation under high pressure. *Nature* **2003**, *423*, 971−974.
(60) Ke, F.; Wang, C.; Jia, C.; Wolf, N. R.; Yan, J.; Niu, S.; Devereaux, T. P.; Karunadasa, H. I.; Mao, W. L.; Lin, Y. Preserving a robust $CsPbI_3$ perovskite phase via pressure-directed octahedral tilt. *Nat. Commun.* **2021**, *12*, 461.
(61) Lee, J.-H.; Jaffe, A.; Lin, Y.; Karunadasa, H. I.; Neaton, J. B. Origins of the pressure-induced phase transition and metallization in the halide perovskite $(CH_3NH_3)PbI_3$. *ACS Energy Lett.* **2020**, *5*, 2174−2181.

https://doi.org/10.1021/jacs.2c10884
J. Am. Chem. Soc. 2022, 144, 23595−23602